Sci. Dril., 35, 21–37, 2026
https://doi.org/10.5194/sd-35-21-2026

Scientific Drilling
Open Access

Recommendations for using core X-ray fluorescence data on basaltic rock as a tool to assess compositional variability

Ashley M. Morris[1], **Sarah Lambart**[1], **Carlos A. Alvarez Zarikian**[2], **John M. Millett**[3,4,5], **Morgan T. Jones**[6], **Sverre Planke**[3,5], **Peter Betlem**[3,7], **Sayantani Chatterjee**[8], **Marialena Christopoulou**[9], **Eric C. Ferré**[10], **Irina Y. Filina**[11], **Joost Frieling**[12,13], **Reed P. Scherer**[14], **Natalia Varela**[15], **Weimu Xu**[16], **and Stacy L. Yager**[17]

[1]MagMaX Laboratory, Department of Geology and Geophysics, University of Utah, Salt Lake City, UT, USA
[2]Scientific Ocean Drilling, Texas A&M University, College Station, TX, USA
[3]Norwegian Geotechnical Institute, Oslo, Norway
[4]Department of Geology and Geophysics, University of Aberdeen, King's College, Aberdeen, UK
[5]Volcanic Basin Energy Research AS, Hoienhald, Oslo, Norway
[6]Department of Ecology, Environment, and Geoscience, Umea University, Umea, Sweden
[7]Department of Arctic Geology, The University Centre in Svalbard (UNIS), Svalbard, Norway
[8]Earthquake Research Institute, The University of Tokyo, Bunkyō, Tokyo, Japan
[9]Sea-Bird Scientific, Bellevue, WA, USA
[10]Department of Geological Sciences, New Mexico State University, Las Cruces, NM, USA
[11]Department of Earth and Atmospheric Sciences, University of Nebraska, Lincoln, NE, USA
[12]Department of Earth Sciences, University of Oxford, Oxford, UK
[13]Department of Geology, Ghent University, Ghent, Belgium
[14]Department of Earth, Atmosphere and Environment, Northern Illinois University, DeKalb, IL, USA
[15]Department of Environmental Sciences, University of Virginia, Charlottesville, VA, USA
[16]School of Earth Sciences and the Research Ireland Centre for Applied Geosciences,
University College Dublin, Dublin, Ireland
[17]Department of Environment, Geology, and Natural Resources, Ball State University, Munice, IN, USA

Correspondence: Ashley M. Morris (ashley.m.morris@utah.edu)

Received: 18 September 2025 – Revised: 23 January 2026 – Accepted: 10 February 2026 – Published: 26 February 2026

Abstract. Portable and core-scanning X-ray fluorescence (XRF) instruments have become increasingly utilized in making rapid, non-destructive chemical characterizations with high spatial resolution on a range of materials. Since basaltic cores are often highly fractured and uneven, portable XRF (pXRF) is preferred to conduct discrete chemical analyses. However, in this case, the user must select the location for each analysis, which can lead to biased datasets. Alternatively, XRF core-scanning (XRF-cs) instruments take a series of measurements along a section of core, increasing the number of analyses and, therefore, eliminating some of the bias introduced by discrete analyses conducted with a pXRF. The XRF-cs does, however, still require a flat sampling surface along the core that does not include void spaces, making rigid, vesicular, and often cracked basalts suboptimal targets. We collected 797 XRF-cs measurements on three basaltic cores collected during the International Ocean Discovery Program Expedition 396 to evaluate how effectively an XRF core scanner can build large, chemically representative datasets. We developed a method for filtering XRF-cs measurements and calibrated the data using discrete calibrated pXRF analyses and compared the XRF-cs data to pXRF and conventional bulk-rock data using various immobile (e.g., Al, Ti, Zr, Ni, Mn, Zn) and mobile (e.g., K, Ca, Sr) elements. The comparison between datasets shows that (1) the XRF-cs data reproduce trends observed by pXRF and conventional bulk-rock data at both the regional scale and the core scale, and (2) in some cases, the higher spatial resolution of the XRF-cs data reveals geochemical variations that are otherwise obscured using discrete analyses. The workflow outlined by this study can be used to select samples for future studies by efficiently providing reliable geochemical data for characterizing new and legacy hard-rock cores.

1 Introduction

In situ X-ray fluorescence (XRF) spectrometry techniques are often used to make rapid, non-destructive chemical characterizations of various materials. These techniques subject materials to high-energy X-rays that remove inner-shell electrons from atoms. These empty inner shells are then filled with outer-shell electrons that shed a portion of their energy, producing X-rays that are characteristic of an element. A detector measures these emitted or fluoresced X-rays that are produced in each energy (kV) range to provide intensity data for each measured element (I_E) that is correlated to the element concentration (Jenkins, 1999; Sitko and Zawisza, 2012). Any material in front of the X-ray beam is measured, including air and dust particles. Therefore, XRF instruments like core scanners that are designed to move along a core and collect many measurements work best when used with samples that have a very flat surface, allowing optimal contact with the X-ray detector. This is why the most predominant geological application for XRF core scanners (XRF-cs) is relatively homogeneous unlithified marine and lacustrine sediment cores (e.g., Richter et al., 2006; Rothwell and Croudace, 2015) where the surface can be gently smoothed and covered by thin films such as 4 µm thick Ultralene plastic (e.g., Reagan et al., 2015a; Johnston et al., 2018; Hahn et al., 2020; Alvarez Zarikian et al., 2024). Since hard rocks are subject to the roughness of their cut surface, void spaces, and cracks, they are more often analyzed with portable-XRF (pXRF) instruments, allowing the user to be more selective about the contact between the beam and a sample. A common procedure is to collect discrete pXRF analyses at regular intervals, such as one to three analyses per core section (i.e., per 0.5–1.5 m; e.g., Jonnalagadda et al., 2024) or per visually identifiable unit (i.e., lava flow, lithofacies; e.g., Reagan et al., 2015a; Planke et al., 2023a) on a homogeneous, representative piece of material. However, collecting pXRF analyses using this method introduces selection bias as each measurement location is decided on by the user. In addition, it is not always possible, even with pXRF, to locate homogeneous analysis locations, which can result in variable X-ray absorption and emission due to porosity and grain size heterogeneity (e.g., Forster et al., 2011). Collecting a higher spatial resolution of analyses with the XRF-cs can reduce the sampling bias and may reveal small-scale heterogeneity while providing a better representation of the average composition of the larger sampling area.

When using XRF instrumentation it is also important to understand the way the data are collected and reported. XRF data are generated as raw spectroscopic data which are then converted and reported as element intensity (in counts per second, cps). The conversion of element intensity (I_E) into a weight proportion ($[E]$) can be described by the following equation (Jenkins, 1999; Sitko and Zawisza, 2012):

$$[E] = I_E \times K \times M + B, \tag{1}$$

where K is a device-specific, empirically derived calibration constant; M describes the total matrix effects; and B is the background intensity. For bulk-rock (destructive) XRF analyses, K and M are usually known. Hence, the concentration of an element can be directly derived from the intensity by applying these two correction factors. However, for in situ XRF-cs data, M is unconstrained as it is affected by variations within samples (e.g., density, grain size, presence of inclusions, core desiccation) and surface irregularities. To at least partly overcome this, XRF-cs raw data are often reported using ratios of element intensities instead of the intensity of a single element (e.g., Pälike et al., 2001; Vlag et al., 2004; Weltje and Tjallingii, 2008; Dunlea et al., 2020) in order to limit matrix effects as the matrix is the same for a single analysis of multiple elements. In some cases, XRF-cs data can also be calibrated into apparent concentrations using standard reference materials or previously calibrated datasets of analyses on the same material (e.g., Jansen et al., 1998; Fisher et al., 2014; Weltje et al., 2015, and references therein; Bourke and Ross, 2016; Kunkelova et al., 2018; Gebregiorgis et al., 2020, Hahn et al., 2020).

Performing XRF-cs measurements on hard-rock cores could improve the sample selection process by quickly generating a larger chemical dataset with reduced sampling bias as compared to traditional pXRF methods. If these data are reliable, this chemical characterization technique would provide better guidance for selecting samples for further study. Using basaltic hard-rock cores collected during the International Ocean Discovery Program (IODP) Expedition 396 (Planke et al., 2023b) as a case study, we investigate a method for collecting XRF-cs geochemical data. In basaltic rocks, elements are often classified as immobile (e.g., Al, Ti, Zr, Ni, Mn, Zn) or mobile (e.g., K, Ca, Sr) to describe their sensitivity to weathering and alteration. Variations in immobile element concentrations record differences in the source composition or degree of fractionation, while variations in mobile element concentrations can indicate altered or weathered rock sections (Smith and Smith, 1976; Pearce and Norry, 1979; Hallberg, 1984; Pearce, 2014; Romano et al., 2024). To evaluate the XRF-cs data collected on the Expedition 396 basalts at the regional scale, we use immobile element ratios of Ti / Zr, Y / Zr, Ni / Mn, and Zn / Mn as these are commonly used as proxies for the fractionation, melting processes, and composition of the mantle source (e.g., Sato, 1977; Sun et al., 1979; Pearce, 2014; Wang et al., 2021; Lang and Lambart, 2022; Bowman and Ducea, 2023). Additionally, we use K / Zr and Sr / Y ratios (mobile and immobile elements) to assess the degree of alteration throughout the cores (Pearce, 2014). Geochemical variation is investigated within holes by plotting chemostratigraphy for uncalibrated element intensity ratios (Ti / Zr, K / Zr, Ni / Mn, Ca / Al) and calibrated immobile (Ti, Ni, Zr) and mobile (Sr) elements. Finally, to determine how representative the chemical variability recorded by the XRF-cs data is of the true chemical variability of the samples, we compare the uncalibrated and calibrated XRF-cs datasets to calibrated pXRF and bulk-rock (conventional bulk XRF analyses and inductively coupled plasma mass spectrometry; ICP-MS) trace element datasets (Tegner et al., 2025). The method outlined by this study is intended to efficiently identify preliminary geochemical trends for large volumes of material. Scientific ocean drilling legacy cores, in particular, amount to many kilometers worth of material that has been collected over the last 50 years alongside technological and scientific developments. As a result, the archived material was not analyzed using a consistent methodology and may therefore contain under-exploited geochemical information relevant to current research initiatives (Super, 2024). Given the scale of these collections, an efficient and systematic method for preliminary geochemical characterization is essential to support informed, targeted sample selection.

2 Case study

The basaltic cores used for this study were collected on the Mid-Norwegian Margin during IODP Expedition 396 in 2021. One of the main objectives of this expedition was to constrain the causes of excess magmatism during the emplacement of the North Atlantic Igneous Province (NAIP) during the opening of the Northeast Atlantic (Planke, et al., 2023b). Basaltic cores were recovered at five different sites: U1566, U1571, U1572, U1573, and U1574. A total of 587 m of basaltic rock was drilled from eight holes, with an average recovery of 61 % (i.e., 357 m). Basaltic units differ between sites with variable thicknesses, vesicularities, crystallinities, and degrees of alteration of the individual lava flows in each unit.

We performed XRF-cs analyses on basaltic cores from three of the five sites from which basaltic rocks were recovered (Fig. S1 in the Supplement). Site U1566 is located on the western flank of the Kolga High, and the basalt sequence of Hole U1566A is characterized by at least 14 discrete basalt flows and 13 inter-basalt-sediment units (Planke et al., 2023c). The basalt flows are mostly composed of aphyric basalt along with a few occurrences of plagioclase–phyric basalt flows. They have highly variable vesicularity and vesicle size distribution, often changing significantly within individual lava flow subunits. Lava flow edges are often characterized by chilled margins, and flow tops are often brecciated with secondary carbonate veins (Planke et al., 2023c). Site U1571 is located on the western side of the Skoll High. Hole U1571A recovered the upper termination of the Inner Seaward Dipping Reflectors (SDRs; Planke et al. 2023b). The top of the first igneous unit in Hole U1571A is composed of a highly altered basaltic andesite that transitions downhole to massive, phaneritic basalt lava flows. The second igneous unit is composed of hyaloclastites and inter-basaltic, volcanic mudstones. The basalts in the second unit range from aphanitic to phaneritic and have highly variable vesicularity. The vesicles in these basalts are often filled by zeolite, clay minerals or white calcite (Planke et al., 2023d). Lastly, Site U1574 targeted basement rock and the overlying sedimentary sequences of the Eldhø Outer High on the northern flank of the Vøring Plateau. The rocks in Hole U1574A include 94 m of pillow basalts and hyaloclastites (Planke et al., 2023e). The top of the first igneous subunit is defined by a hydrothermal breccia which overlies a short interval of plagioclase–phyric pillow basalt and a hyaloclastite. A second subunit begins as a hyaloclastite interval before transitioning to aphyric basalt. Both subunits observed are mostly composed of plagioclase–phyric basalt, highly vesicular and sparsely vesicular aphyric aphanitic basalt, and massive aphyric phaneritic basalt. The pillow basalt sections often have rounded vesicles filled with clay minerals; zeolites; calcite; and, occasionally, sulfide (Planke et al. 2023e).

3 Methods

3.1 Shore-based XRF core scanning

XRF-cs analyses were performed on the archive core halves from Expedition 396 Holes U1566A, U1571A, and U1574A with the Avaatech energy-dispersive XRF core scanner (Fig. 1A) at the IODP Texas A&M facilities of College Station, Texas. Energy-dispersive XRF instruments prioritize the collection of many elements by measuring all fluoresced X-ray energies simultaneously before separating them electronically (Drake et al., 2022). The XRF-cs requires a flat, level sample surface to make optimal contact and avoid measuring air. Due to the nature of the hard rock (fractured, solid), the traditional core-scanning technique used on sediments was modified to optimize the quality of the data. Rather than measuring at regular intervals (e.g., 1 cm), all rock fragments which were large enough for the sample irradiation area were identified, raised, and leveled within the core liner using moldable clay protected by Kimtech wipes to prevent contamination (Fig. 1B). The sample irradiation area is 10 mm in the downcore direction and 12 mm in the cross-core direction (e.g., Alvarez Zarikian et al., 2024). The intervals of the identified fragments were measured at the mil-

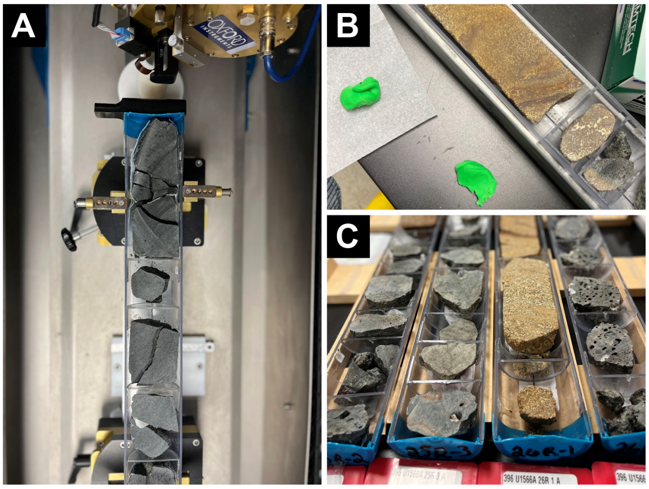

Figure 1. **(A)** A core section loaded into the core scanner; the XRF, located at the top of this photo, moves down over the core and stops to analyze at locations entered into the software. **(B)** Moldable clay and Kimtech wipes used to level hard rocks in the core liner. **(C)** Heterogeneous core sections from Hole U1566A that have been leveled with moldable clay in the core liners.

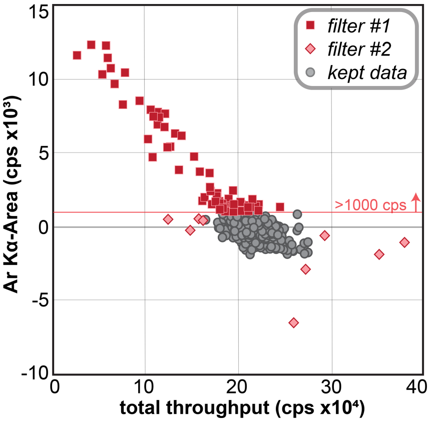

Figure 2. Kα-peak area intensity (counts per second, cps) of Ar plotted against the total throughput to show how the raw XRF-cs data are filtered. Filter no. 1 refers to any analyses with Ar cps > 1000. Filter no. 2 refers to outliers (3σ).

limeter scale to be analyzed so that pieces with insufficient surface areas could be avoided. It should be noted that this process eliminates rock samples that are small, fragile, or unconsolidated, as well as those with a high volume of cavities and vesicles, from being measured, introducing some inherent bias. At each measured location, the core scanner takes three measurements at three different voltages so that it is optimized to collect a full spectrum of elements (10 kV = Mg, Al, Si, P, S, Cl, Ar, K, Ca, Ti, Cr, Mn, Fe; 30 kV = K, Ca, Ti, Mn, Fe, Co, Ni, Cu, Zn, Ga, As, Br, Rb, Sr, Y, Zr, Nb, Mo; and 50 kV = Ca, Fe, Ni, As, Br, Sr, Y, Zr, Nb, Mo, Ag, Ba). However, variations in the input voltage affect the depth to which X-rays interact with the material and different elements, therefore changing the amount of material measured (Hubbell and Seltzer, 2004; Drake et al., 2022). Since all elements used in the following discussion fall within the 30 kV range, only the 30 kV spectrum is used, although the use of element ratios may allow users to compare elements collected at different voltages in future applications.

Positive measurements of argon (Ar) indicate that air was measured in the analysis as Ar is the only element in air that can be reliably measured by the core scanner (Drake et al., 2022). Accordingly, measurements of Ar were used to identify analyses affected by poor contact with the instrument detector. The data were filtered in two steps: (1) analyses with Ar counts greater than 1000 were removed from the dataset, and (2) analyses for which total spectrum throughput (counts per second, cps) or Ar counts fell outside of the 3 standard deviations were considered to be outliers and were removed from the dataset (Fig. 2). All analyses are reported in Table S1. After filtering, we obtained 293 analyses of basalt from 47.7 m of recovered core length (31.4–145.8 m of core below the seafloor [m CSF-A]) of the U1566A core, 189 analyses from 29.4 m of recovered core length (200.4–242.3 m CSF-A) of the U1571A core, and 237 analyses from 40.0 m of recovered core length (166.8–258.7 m CSF-A) of the U1574A core. Sample locations were collected and reported in terms of m CSF-A.

3.2 Calibrating XRF-cs data with pXRF data

Standard reference materials (SRMs) for XRF techniques are often powdered and homogenized, raising some concern over whether comparisons with heterogeneous rock surface measurements are valid due to the variability of matrix effects (Fisher et al., 2014). While some studies show no significant difference between XRF analyses performed on cut rock surfaces and powered samples (Ryan et al., 2017; Johnston et al., 2018), others highlight the importance of sample homogeneity on analytical precision (Fisher et al., 2014; Bourke and Ross, 2016). As an alternative to using SRMs, XRF-cs intensity data may be converted into apparent concentrations of individual elements if a subset of calibrated data is available (i.e., Gebregiorgis et al., 2020; Hahn et al., 2020). Calibrated, discrete pXRF analyses collected on the archive half of the core during the expedition using an Olympus Delta handheld pXRF spectrometer are available for the basaltic cores used in this study (Tegner et al., 2025). Details on the acquisition of the pXRF analyses are provided by Planke et al. (2023a). In brief, the pXRF analyses were carried out directly on the surface of the core. Three analyses were performed for each data point. In addition to the internal calibrations of the instrument, calibration curves for the different elements measured via pXRF were determined using a suite of 10 standard reference materials chosen to cover the expected range of compositions and matrices for the analyzed samples.

Elements falling below the limit of detection on samples and elements which produced calibrations curves with R^2 values lower than 0.95 were discarded. After filtering, analyses on the following elements are considered to be quantitative: Ca, K, Ti, Fe, Mn, Ni, Cr, Cu, Zn, Sr, Rb, Zr, and Y (Tegner et al., 2025). By using these pXRF data to calibrate the XRF-cs data, we avoid introducing additional matrix differences (Fisher et al., 2014) into our calibration as the analyses are collected on the same rocks. We note, however, that, for future applications for which a suitable subset of calibrated data is not available, users may calibrate XRF-cs data with a suite of SRMs following the procedures specified for the pXRF data (Planke et al., 2023a).

Bulk-rock major and trace element analyses were also performed following the expedition by conventional XRF and ICP-MS techniques on the working core halves (Tegner et al., 2025; see also Morris et al., 2024, for methodology). We used quantitative pXRF analyses to calibrate the XRF-cs data rather than the bulk-rock data for two reasons: (1) both the pXRF and XRF-cs data were acquired on the archive core halves, while the bulk-rock data were acquired on the working halves, reducing the potential for physical offset in analysis locations, and (2) the goal of this paper is to evaluate if XRF-cs data collected on basaltic cores can be used to guide the selection for a post-expedition study and, if so, to provide a workflow. Hence, in future studies, XRF-cs data would be collected prior to conventional, destructive bulk-rock analyses which are only used in this study to validate the trends observed within the pXRF and XRF-cs datasets. The calibration of the XRF-cs data was performed following the method outlined by Gebregiorgis et al. (2020), which uses the robust regression model from the Statistics toolbox in MATLAB (R2021b) to correlate pXRF data (in $\mu g\, g^{-1}$) in relation to XRF-cs data (in cps). Robust regression is preferred for this method over a linear regression model as it does not assume that the error distribution is Gaussian (Fig. S2; Gebregiorgis et al., 2020, and references therein). To apply this method, analyses from the pXRF and XRF-cs datasets were selected to match sampling locations (in m CSF-A) to within 1 cm of each other (Tables S1 and S2). Additionally, individual element values which fell outside the 2 standard deviations of the mean cps $(\mu g\, g^{-1})^{-1}$ are not included in the regression. Regressions are calculated using 35 individual XRF-cs/pXRF data pairs (13, 8, and 14 pairs for Holes U1566A, U1571A, and U1574A, respectively). Elements that were successfully calibrated to apparent concentrations include Ca, K, Ti, Fe, Mn, Ni, Cu, Zn, Sr, Y, and Zr. Calibration curves are shown in Fig. S2, and the calibrated apparent concentrations are reported in Table S1. Other elements were either not measured by pXRF (e.g., Co, Ga, As, Br, Mo, Ag), had insufficient concentrations to calculate a regression (e.g., Rb, Nb), or were not well calibrated using pXRF data (Mg, Al, Si; Planke et al., 2023a).

3.3 Statistical analysis

Uncalibrated element intensity ratios and calibrated element concentration ratios from the XRF-cs datasets were compared between holes to evaluate the ability of each dataset to identify large-scale, regional trends. These ratios were similarly investigated using 241 pXRF and 60 bulk-rock (conventional XRF and ICP-MS) analyses (Tegner et al., 2025). Analysis of variance (ANOVA) and Tukey honestly significant difference (HSD) statistical tests were performed for each element intensity ratio to determine if the differences between Holes U1566A, U1571A, and U1574A are statistically significant for each dataset. The ANOVA test evaluates all sites together, while the Tukey HSD test evaluates between individual sites; hence, the Tukey HSD test is only performed when the ANOVA test indicates no statistical difference. These tests were performed in Python (3.12) using the f_oneway() (ANOVA) and tukey_hsd() (Tukey HSD) functions in the scipy.stats package (Virtanen et al., 2020). The p values calculated for the ANOVA and Tukey HSD tests for each element intensity ratio and dataset are reported in Table 1, and the full outputs (i.e., F-statistic, confidence intervals) are reported in Table S3.

4 Results

4.1 Regional variations

The first column in Fig. 3 presents uncalibrated intensity ratios for analyses collected on all three basaltic cores. Basalts from Hole U1571A have lower Y / Zr and K / Zr and higher Sr / Y values than the basalts from the other two holes. Basalts from Hole U1566A show higher K / Zr intensity ratios and present overall lower Ni / Mn and Zn / Mn intensity ratios. The ANOVA and Tukey HSD results (Table 1) indicate that the visually observable (Fig. 3) differences between the Y / Zr, Ni / Mn, Zn / Mn, and K / Zr ratios in the basalts for each hole are statistically significant ($p \ll 0.05$) for the uncalibrated XRF-cs intensity ratios (Siegel and Wagner, 2022). The Ti / Zr and Sr / Y values between Holes U1566A and U1574A are statistically similar ($p > 0.05$) but are otherwise significantly different between the other holes.

The middle column of Fig. 3 presents the same ratios calculated using calibrated XRF-cs data. While some features persist after the calibration, such as the distinctive K / Zr, and Sr / Y ratios of basalts from U1571A, the basalts from U1566A and U1574A show more overlap. This is consistent with the ANOVA and Tukey HSD results, which indicate that no statistical difference is observed between Holes U1566A and U1574A for these ratios (Table 1). Additionally, the Ni / Mn ratios that appear to be different between the U1566A and U1571A basalts are now clearly overlapping. Table 2 reports the average values for these ratios and their associated 1 standard deviation (1σ).

Table 1. p values calculated for ANOVA and Tukey HSD tests comparing regional geochemistry. The XRF-cs raw dataset uses the uncalibrated element intensity ratio, and the XRF-cs cal dataset uses the calibrated element concentration ratios.

Dataset	Holes	Test	Ti / Zr	Y / Zr	K / Zr	Sr / Y	Ni / Mn	Zn / Mn
XRF-cs raw	all	ANOVA	0.000	0.000	0.000	0.000	0.000	0.000
XRF-cs raw	U1566A-U1571A	Tukey HSD	0.000	0.000	0.000	0.000	0.000	0.000
XRF-cs raw	U1566A-U1574A	Tukey HSD	**0.999**	0.001	0.000	0.000	0.000	**0.309**
XRF-cs raw	U1571A-U1574A	Tukey HSD	0.000	0.000	0.022	0.000	0.007	0.000
XRF-cs cal	all	ANOVA	0.007	0.000	0.000	0.003	0.000	0.000
XRF-cs cal	U1566A-U1571A	Tukey HSD	0.027	0.000	0.000	**0.235**	0.000	0.000
XRF-cs cal	U1566A-U1574A	Tukey HSD	**0.819**	0.001	0.042	**0.092**	0.000	**0.950**
XRF-cs cal	U1571A-U1574A	Tukey HSD	0.008	0.000	0.000	0.002	0.011	0.000
pXRF	all	ANOVA	0.042	0.000	0.009	0.000	**0.094**	0.000
pXRF	U1566A-U1571A	Tukey HSD	**0.063**	0.000	0.006	0.000		0.002
pXRF	U1566A-U1574A	Tukey HSD	**0.995**	**0.353**	**0.617**	**0.908**		0.002
pXRF	U1571A-U1574A	Tukey HSD	**0.126**	0.000	**0.815**	0.000		**1.000**
ICP-MS	all	ANOVA	**0.086**	0.000	0.034	**0.437**	**0.927**	0.000
ICP-MS	U1566A-U1571A	Tukey HSD		**0.979**	**0.863**			0.000
ICP-MS	U1566A-U1574A	Tukey HSD		0.000	0.032			**0.742**
ICP-MS	U1571A-U1574A	Tukey HSD		0.000	**0.084**			0.001

Bolded values indicate p values of > 0.05 and suggest no statistically significant difference between the tested groups (see Sect. 5.1 for details).

Table 2. Averages of the concentration ratios and associated standard deviations (1σ) obtained used the ICP-MS, pXRF, and calibrated XRF-cs datasets for each hole.

		Ti / Zr		Y / Zr		K / Zr		Sr / Y		Ni / Mn		Zn / Mn	
Dataset	Hole	Avg	1σ	Avg	1σ	Avg	1σ	Avg	1σ	Avg	1σ	Avg	1σ
XRF-cs cal	U1566A	101.4	14.2	0.53	0.12	40.6	10.5	3.4	4.5	0.07	0.03	0.06	0.02
XRF-cs cal	U1571A	105.0	8.3	0.28	0.04	20.1	2.6	5.8	1.2	0.06	0.02	0.08	0.02
XRF-cs cal	U1574A	100.7	8.6	0.51	0.09	38.6	7.6	3.4	0.5	0.07	0.02	0.08	0.02
pXRF	U1566A	99.9	13.4	0.49	0.06	5.2	24.1	2.8	2.9	0.10	0.17	0.06	0.06
pXRF	U1571A	104.9	19.1	0.29	0.05	29.9	21.6	5.6	1.6	0.07	0.02	0.09	0.04
pXRF	U1574A	99.6	7.9	0.48	0.07	40.7	1.5	3.0	0.3	0.06	0.03	0.08	0.02
ICP-MS	U1566A	109.6	13.6	0.47	0.08	27.8	15.0	2.9	2.0	0.13	0.20	0.06	0.10
ICP-MS	U1571A	101.8	11.1	0.27	0.05	23.2	44.4	5.3	1.2	0.06	0.04	0.07	0.02
ICP-MS	U1574A	107.7	9.5	0.47	0.06	18.0	7.6	3.3	0.4	0.05	0.01	0.06	0.02

The right column of Fig. 3 presents the quantitative pXRF and bulk-rock datasets acquired on the same basaltic cores. Because only a small subset of pXRF data was used to calibrate the XRF-cs data, the comparison between the two datasets provides an evaluation of the robustness of the calibration. Since the bulk-rock data were acquired on the working halves of the cores, these provide an additional, independent test. By comparing the XRF-cs datasets (uncalibrated and calibrated) and the pXRF and bulk-rock datasets, we can make a series of observations: (i) all four datasets indicate significant differences between Holes U1566A and U1571A and between Holes U1571A and U1574A for the ratio Sr / Y. (ii) The Tukey HSD tests for Ti / Zr on the XRF-cs datasets indicate significant differences, like those of the Sr / Y values, while pXRF and ICP-MS datasets suggest that all three holes overlap. (iii) Each dataset distinguishes K / Zr and Zn / Mn differently between the holes; uncalibrated XRF-cs data indicate that all sites are different for these ratios, while pXRF and bulk-rock data show more overlap, with disagreement between holes. (iv) While uncalibrated XRF-cs data show significant Ni / Mn ratios between each hole, the calibrated XRF-cs data suggest larger overlap, consistently with statistical tests on pXRF and bulk-rock datasets.

4.2 Chemical stratigraphy

Figures 4 and 5 show chemical stratigraphy (element or element ratio vs. m CSF-A) for Hole U1566A. The correspond-

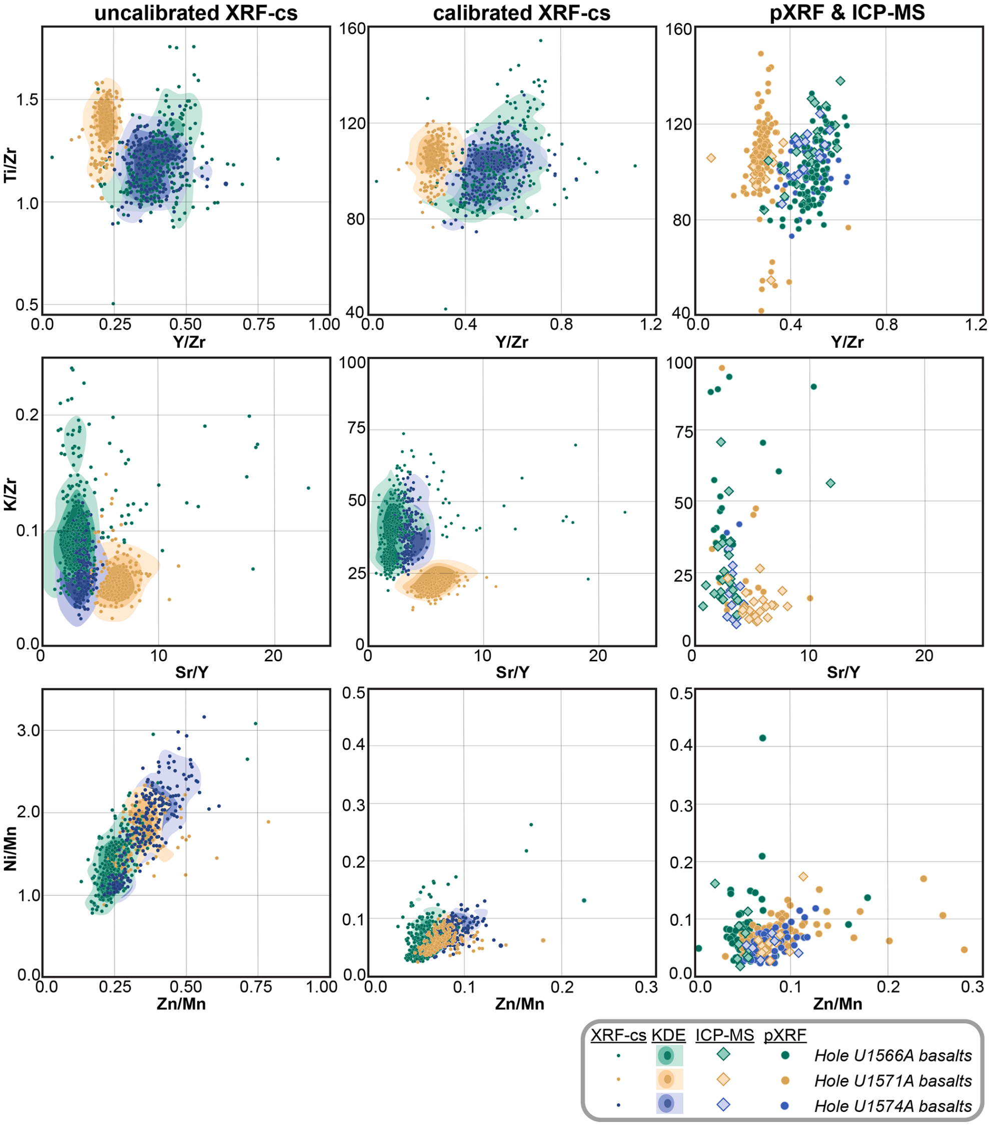

Figure 3. Element ratios for data collected on all three basaltic cores. The left column shows the uncalibrated XRF-cs dataset with ratios of elemental intensity (Table S1). The middle column shows the calibrated XRF-cs dataset with ratios of elemental concentrations (Table S1). For the XRF-cs data, kernel density estimations (KDEs) are also plotted. The right column shows the quantitative pXRF and ICP-MS elemental ratios (Tegner et al., 2025) for each site.

ing figures for Holes U1571A and U1574A are available in the Supplement (Figs. S3 and S4). The uncalibrated data were plotted using ratios of element intensity for Ti / Zr, Sr / Y, Ni / Mn, and Ca / Al (Fig. 4), and the calibrated data were plotted as concentrations of the elements Ti, Sr, Ni, and Zr (Fig. 5) to compare immobile and mobile element variations between the datasets. Both the uncalibrated and calibrated XRF-cs datasets are compared with the pXRF and bulk-rock data (Tegner et al., 2025); we note that bulk-rock data were collected on the archive halves, and so analyses may not be directly comparable as the relative distance to the top of the core may be slightly shifted. The geochemical trends in the pXRF and bulk-rock data broadly agree with downhole variability of the XRF-cs data (Figs. 4 and 5). In some sections, however, the XRF-cs data highlight more variability than the other datasets. Some notable chemical anomalies that can be more clearly observed by the XRF-cs data indicate lithological changes like brecciated basalts (positive Ti, Zr, and Ti / Zr at 37.38 m CSF-A; Figs. 4 and 5), alternating aphyric basalt and phyric plagioclase basalt (72.29–74.12 m CSF-A; Figs. 4 and 5), and a pyroclastic unit (positive Ni and Ni / Mn at 66.13 m CSF-A; Figs. 4 and 5). A few positive Sr anomalies in XRF-cs apparent concentrations, as well as positive Sr / Y and Ca / Al anomalies in the XRF-cs intensity ratios, highlight a section of continuous aphyric basalt (90.98–98.99 m CSF-A; Figs. 4 and

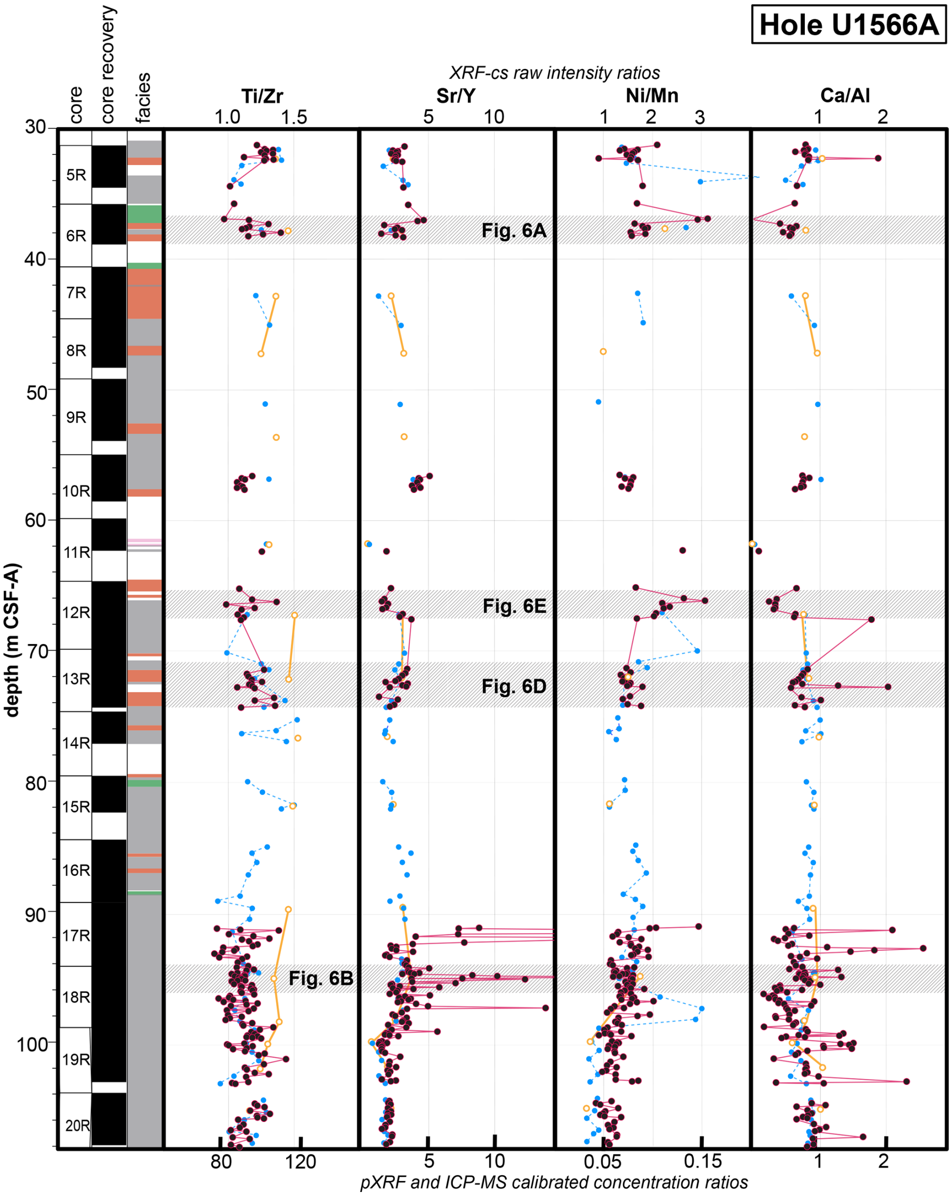

Figure 4.

5). A second section of aphyric basalt further downhole is characterized by multiple positive Sr (and Sr / Y) anomalies and increasing Ti and Zr calibrated concentrations (135.09–141.07 m CSF-A; Figs. S3 and S4). Chemical stratigraphy for Hole U1571A and U1574A basalts further highlights chemical anomalies within sections with little to no facies variations (Figs. S3 and S4).

5 Discussion

The ability to collect a large chemical dataset over a relatively short period of time without damaging the samples can greatly assist in the sample selection process for further detailed (destructive) analyses, especially under time-sensitive conditions. The importance of developing techniques that enhance the core characterization process was recently highlighted by the Scientific Ocean Drilling 2050 Science Framework (Koppers and Coggon, 2020) as the community adjusts to changes in the IODP. These techniques may be particularly helpful to apply to the large quantities of legacy core material that may have less available information due to variations to the standard procedure and to the technology available to oceanic core collection over time (Super, 2024). Additionally, the geoscience community has recognized that, regardless of the use of published classification schemes, lithological characterization can be biased by the scientist making

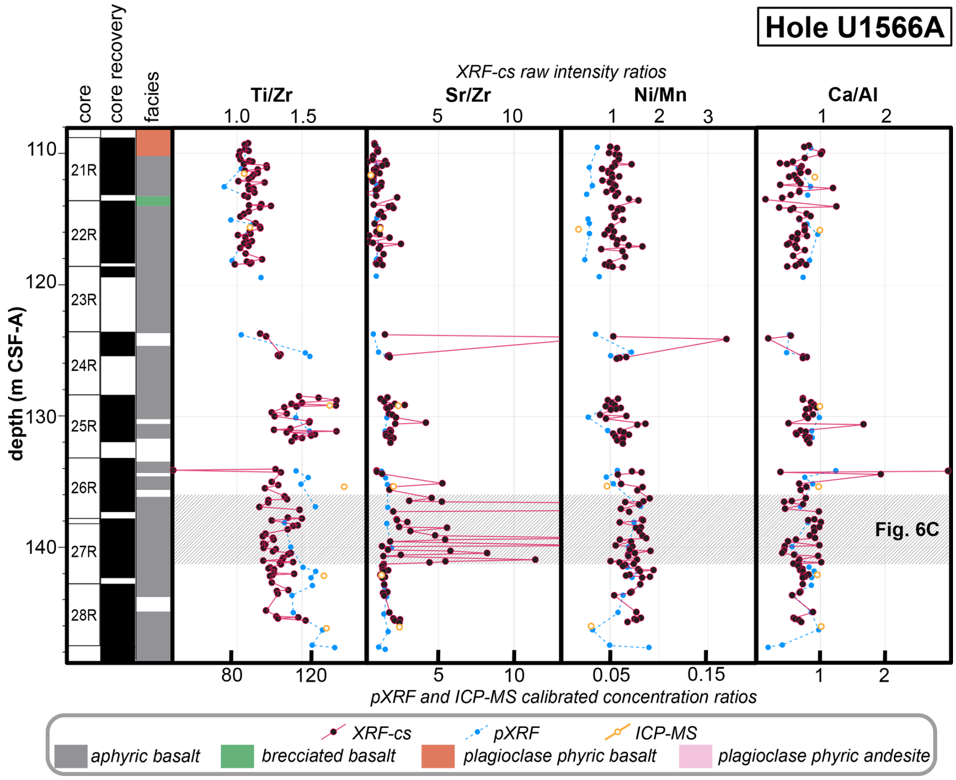

Figure 4. Chemical stratigraphy for Ti / Zr, Sr / Y, Ni / Mn, and Ca / Al element intensity (cps) ratios for Hole U1566A basalts measured by the XRF-cs. The pXRF and ICP-MS concentration (µg g^{-1}) ratios (Tegner et al., 2025) are also plotted. The depth scale, CSF-A, corresponds to meters of core below the seafloor. Hatched gray sections indicate sections of core discussed in the text, with corresponding core photos in Fig. 6. Lithofacies are from the shipboard IODP Expedition 396 observations, and blank intervals indicate intervals of no core recovery or thin sedimentary layers (Planke et al., 2023c).

observations (e.g., Lokier and Al Junaibi, 2016; Fresia et al., 2017; Dawson et al. 2023). One approach suggested to standardize this process is to use neural networks and machine learning; however, these work best when trained with large datasets (Dawson et al., 2023). A high resolution of carefully managed XRF-cs chemical data may be a useful tool for effectively training neural networks to quickly and accurately classify basaltic hard-rock cores. Whether for training large datasets or for being applied to a specific suite of samples to assist in sampling for a particular study, using XRF-cs may become a valuable tool for many future hard-rock core studies. Below, we discuss the reliability of the XRF-cs dataset collected for the three IODP basaltic cores in our case study from Holes U1566A, U1571A, and U1574A using comparisons between the holes to investigate regional chemical trends and chemical stratigraphy to investigate chemical variability within holes.

5.1 Regional variations

Chemical differences observed in basalts from different sites can be important indicators of regional trends. In particular, chemical differences between the basaltic cores recovered during IODP Expedition 396 may reflect changes that occurred during the formation of the Northeast Atlantic. In fact, the three sites studied here have been interpreted to correspond to three stages of rifting processes (Planke et al., 2023b): the initiation of rifting in a subaerial environment (Site U1566); the top of the seaward dipping reflectors, interpreted as the end of the peak of magmatic activity (Site U1571); and a late-stage shallow marine volcanic eruption (Site U1574). A good characterization of the compositional ranges and variations observed between sites is consequently crucial to better understand mantle and crustal processes (e.g., mantle source composition, mantle melting, magma–crust interaction, and crustal contamination or shallow fractionation processes) that occur during continental breakup (e.g., Meyer et al., 2009; Morris et al., 2024; Tegner et al. 1998).

When observing the regional variation between these basalts, the uncalibrated and calibrated XRF-cs datasets do not always agree. The ratios plotted in Fig. 3 exemplify three cases that can be used to outline the limitations and precautions of using XRF-cs data. The first case is shown by means of the regional distribution of the immobile element ratios, Ti / Zr and Y / Zr, which are similar between the

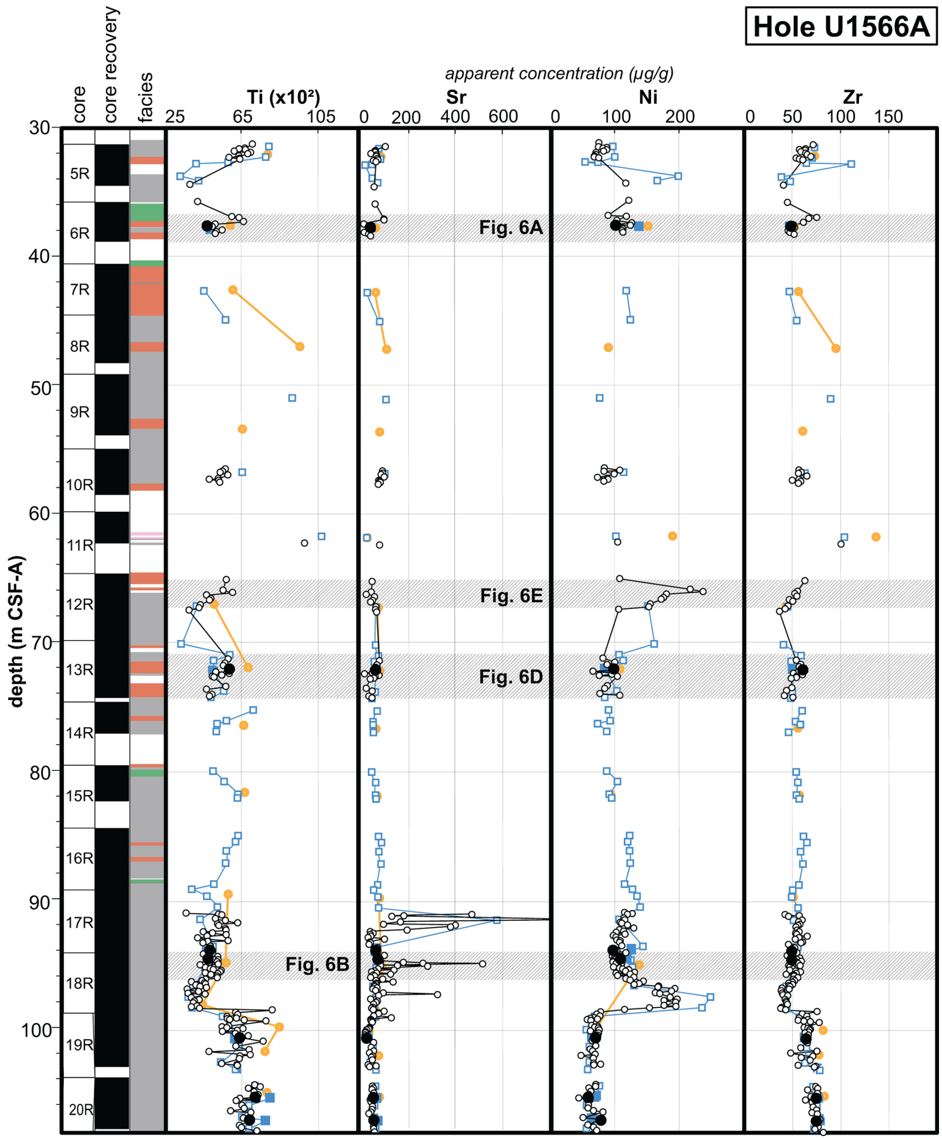

Figure 5.

XRF-cs calibrated and uncalibrated data. These ratios show more overlap between Holes U1566A and U1574A than with Hole U1571A basalts that have lower Y / Zr values and a more confined range of Ti / Zr values. For both datasets, the ANOVA and Tukey HSD tests indicate that the Y / Zr values are significantly different ($p \ll 0.05$) between each hole and that Ti / Zr values are only the same ($p > 0.05$) for Holes U1566A and U1574A (Table 1). These results suggest that there is no notable difference between the uncalibrated and calibrated XRF-cs datasets when comparing regional trends for these immobile elements that are well calibrated (Fig. 3). Additionally, the pXRF and destructive bulk-rock data show the same regional trends as the XRF-cs datasets (Fig. 3). However, the statistical tests indicate that Ti / Zr values are the same across all three holes, and the results for Y / Zr indicate that the values are the same for Holes U1566A and U1574A according to pXRF data and for Holes U1566A and U1571A according to ICP-MS data (Table 1).

The K / Zr ratio exemplifies a second case in which the uncalibrated XRF-cs data seem to agree with pXRF and bulk-rock data better than the calibrated data. The uncalibrated data show that the basalts from Hole U1566A have higher and more diverse K / Zr ratios (Fig. 3), which is reflected by the statistical tests that indicate that these values are significantly different ($p \ll 0.05$) between the basalts from each hole (Table 1). This agrees with the results observed in the pXRF and bulk-rock data, except the Tukey HSD test results for pXRF, which indicate that K / Zr is not significantly different ($p > 0.05$) between Holes U1566A and U1574A and between Holes U1571A and U1574A (Table 1). The

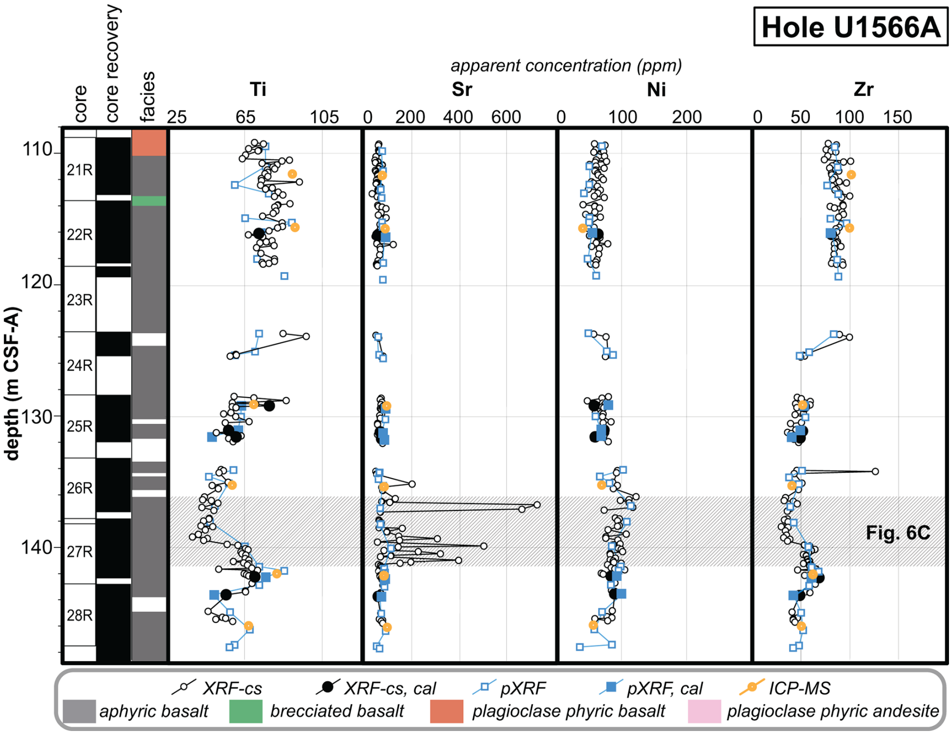

Figure 5. Ti, Sr, Ni, and Zr calibrated concentration ($\mu g\, g^{-1}$) chemical stratigraphy plots for the U1566A basalts using XRF-cs calibrated concentrations. Concentrations obtained by means of pXRF and ICP-MS (Tegner et al., 2025) are also plotted. For the XRF-cs and pXRF data, "cal" denotes analyses that were used to calculate the calibration curves (Fig. S2). Hatched gray sections indicate sections of core discussed in the text, with corresponding core photos in Fig. 6. Lithofacies are from the shipboard IODP Expedition 396 observations, and blank intervals indicate intervals of no core recovery or thin sedimentary layers (Planke et al., 2023c). Concentrations are in $\mu g\, g^{-1}$.

calibrated data, instead, show more overlap between Holes U1566A and U1574A, supported by the Tukey HSD test results (Fig. 3, Table 1), with the K / Zr ratios for Hole U1574A plotting systematically above the values of 20 (Fig. 3), while the average value obtained by bulk-rock data is 18 ± 8 (1σ). The discrepancy between the calibrated XRF-cs data and the pXRF and bulk-rock data, however, can be explained by the low number of K analyses obtained by pXRF. In fact, K concentrations obtained by pXRF were often below the detection limit. The methodology to select XRF-cs and pXRF pairs for calibrations (see Sect. 3.2) resulted in only three K analyses being available for calibration. These results highlight that, despite the good calibration obtained for K_2O on pXRF data (Planke et al., 2023a; Tegner et al., 2025), the very limited number of data available in the pXRF dataset ($n = 3$) does not allow for a robust calibration of XRF-cs data (Fig. S2). Alternatively, the results for Sr / Y, which is also a mobile–immobile element ratio, agree very well across all four datasets, suggesting that the variable results from K / Zr are unrelated to the mobility of K.

While it can be tempting to use uncalibrated ratios to make preliminary qualitative observations about regional variability, a third case, exemplified by Ni / Mn and Zn / Mn, highlights the need for caution with this approach. In the uncalibrated XRF-cs data, Ni / Mn and Zn / Mn values show a progressive increase in basalts from Hole U1566A to U1571A to U1574A basalts. However, the calibrated data show more tightly clustered values (Fig. 3), a fact which aligns more closely with trends seen in both the pXRF and bulk-rock data (Fig. 3). This is further supported by statistical tests: while the uncalibrated XRF-cs ratios are significantly different ($p \ll 0.05$) across the holes, the calibrated XRF-cs, pXRF, and bulk-rock data show far less statistical variation, particularly for Ni / Mn (Table 1). Although the uncalibrated element intensity ratios may sometimes appear to reflect real trends, the relationship between intensity and concentration is non-linear (Weltje et al., 2015). Therefore, regional variations seen in the uncalibrated data can be misleading, outlining the importance of only using well-calibrated data to interpret regional geochemical variations.

Comparisons between datasets

Both the uncalibrated and calibrated XRF-cs datasets indicate more significant differences between the basalts from each hole compared to the smaller pXRF and bulk-rock datasets (Table 1). This may seem counterintuitive as one might expect the larger amount of data in the XRF-cs datasets to show more overlap between sites relative to the traditional pXRF and ICP-MS datasets. In fact, the bulk-rock and pXRF datasets represent only 9 % and 37 %, respectively, of the size of the XRF-cs dataset. We interpret the results of the statistical tests as evidence supporting the fact that the XRF-cs data collection effectively reduces sample selection bias for hard-rock core measurements and that the observed regional trends are true to the chemical variability of the basalts. For example, fresh and homogeneous samples are usually preferred for bulk-rock data analyses, which could be contributing to the observation of fewer regional differences between the holes. Similarly, pXRF analysis locations are often selected to represent a specific section, unit, or facies and are positioned away from altered material. In contrast, XRF-cs analysis locations include any material that makes optimal contact with the detector. Hence, after filtering and calibration, the statistical differences observed within this higher-spatial-resolution dataset can be considered to be robust features reflecting the true regional variability in basalt compositions.

5.2 Small-scale variability

Studying the chemical variations along a rock core can highlight characteristic trends that can assist in sample selection for a variety of studies. Chemical stratigraphy plots are routinely constructed for IODP Expedition reports with the ICP atomic emission spectrometry and pXRF data collected on board to supplement post-expedition sampling (i.e., Reagan et al., 2015b; Planke et al., 2023c–e). Here, we discuss how uncalibrated XRF-cs intensity ratios (Fig. 4) and calibrated XRF-cs elemental concentrations (Fig. 5) compare with the pXRF and bulk-rock data (Tegner et al., 2025). Since the methods tested here are intended to guide sample selection prior to destructive analysis, the bulk-rock data are only used as an independent test for the accuracy of the chemical variability observed in the XRF-cs data.

In general, the pXRF and bulk-rock chemical stratigraphy show the same trends as the uncalibrated and calibrated XRF-cs datasets. Importantly, the high spatial resolution of the XRF-cs dataset compared to the pXRF dataset highlights chemical variations along the cores that are not always observable by the discrete pXRF data alone. In the following discussion, anomalies within the chemical stratigraphy are discussed as the percent change relative to the nearest analyses taken in the above stratigraphy. No significant anomalies correspond to a less than 30 % change, while small and large anomalies are defined as resulting in 30 %–100 % change and more than 100 % change, respectively. In some cases, the XRF-cs data simply identify visually recognized variations, such as discrete inclusions, lithofacies changes, or sediment layers. For example, a brecciated basalt in core U1566A-6R2 (37.00 m CSF-A; Fig. 6A) is highlighted by small positive anomalies in Ti, Sr, and Zr (41.9 %, 51.8 %, and 67.7. % change, respectively), and a deeply altered, leucocratic pyroclastic layer in core U1566A-12R1 (66.94 m CSF-A; Fig. 6E) is highlighted by a large positive Ni anomaly (103.1 % change; Fig. 4). The XRF-cs data can also record the presence of large vesicles filled by secondary minerals, like in core U1566A-17R4 (90.97–98.99 m CSF-A; Fig. 6B), which is identified by eight large positive Sr anomalies, with increases ranging between 114.4 % and 737.4 % (Figs. 4 and 5).

While the uncalibrated and calibrated XRF-cs chemical stratigraphy highlights many of the same anomalies, the scale of the uncalibrated element intensity ratios can sometimes be misleading. For example, the chemical stratigraphy for Ni / Mn shows a small positive anomaly (84.9 % change) for the brecciated basalt (37.00 m CSF-A; Figs. 4 and 6A) that is not observed by the Ni calibrated concentration chemical stratigraphy (Fig. 5). Conversely, there is a gradual increase in calibrated Ni at 96.87 m (CSF-A, Fig. 5) that is not observed in the uncalibrated Ni / Mn chemical stratigraphy (Fig. 4). The pXRF data show the same gradual increase at this depth for both Ni concentrations and Ni / Mn ratios. This suggests that, when possible, using well-calibrated XRF-cs data is also preferred for investigating small-scale chemical variation.

XRF-cs data can also be used to demonstrate that compositional variability is not necessarily correlated with facies variations. Figure 7 compares the calibrated chemical stratigraphy for two sections of core, both being about 4 m long, from Hole U1566A in more detail. Core section U1566A-27R2 (139.2–140.67 m CSF-A) shows little to no variation in its lithofacies (Fig. 6C), while core section U1566A-13R3 (71.28–74.16 m CSF-A) is composed of seven different units, including aphyric basalt, plagioclase–phyric basalt, and sediments (Fig. 6D). However, the XRF-cs chemical stratigraphy for section U1566A-27R2 reveals variability in the Sr concentration, including five large positive anomalies, with increases ranging between 108.4 % and 740.9 %, that were not recorded by the pXRF analyses (Fig. 7A). The Ti chemical stratigraphy for this section also shows a distinct step which may indicate a boundary between chemically distinct lava flows, recorded by the pXRF data as a gradual increase (Fig. 7A). In contrast, core section U1566A-13R3 shows low chemical variability within the XRF-cs and pXRF data despite the large variability in its facies (Fig. 7B). Core section U1566A-27R2 does present small, filled vesicles (Fig. 6C), but, because they are consistent throughout the core, we may not necessarily expect them to result in the scale of geochemical variability observed. The high Sr concentration may potentially result from vesicles being filled with carbonate-bearing material, and identifying these minerals prior to analyses can be useful for further study (e.g., potential for carbon sequestration, interpretation of isotopic ratios).

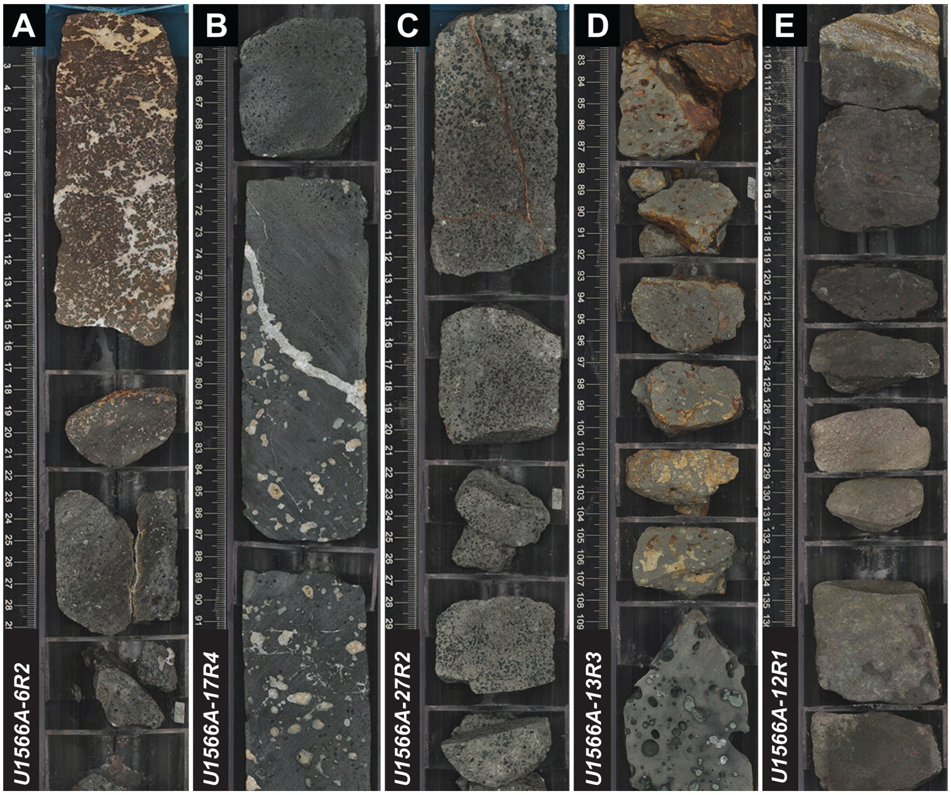

Figure 6. Photos of representative pieces within core sections described in the text. **(A)** U1566A-6R2 (37.38–38.31 m CSF-A), a section of brecciated basalt that transitions into plagioclase phyric basalt. **(B)** U1566A-17R4 (93.82–95.14 m CSF-A) is a section of continuous aphyric basalt with re-mineralized inclusions that could be the cause of elemental variations seen in the chemical stratigraphy (Figs. 4 and 5). **(C)** U1566A-27R2 (139.29–140.67 m CSF-A) is a section of aphyric basalt that is relatively visually homogeneous but has variable elemental concentrations (Fig. 7). **(D)** U1566A-13R3 (72.53–73.63 m CSF-A) is a representative section with high lithofacies variability that is compared to panel **(C)** in Fig. 7. **(E)** Section U1566A-12R1 (65.12–66.13 m CSF-A) has an interlayer of pyroclastic material from 126 to 139 cm between plagioclase phyric basalt above and aphyric basalt below. Photos of the full core sections represented by the data presented within Figs. 4 and 5 can be found in the Supplement (Morris et al., 2026).

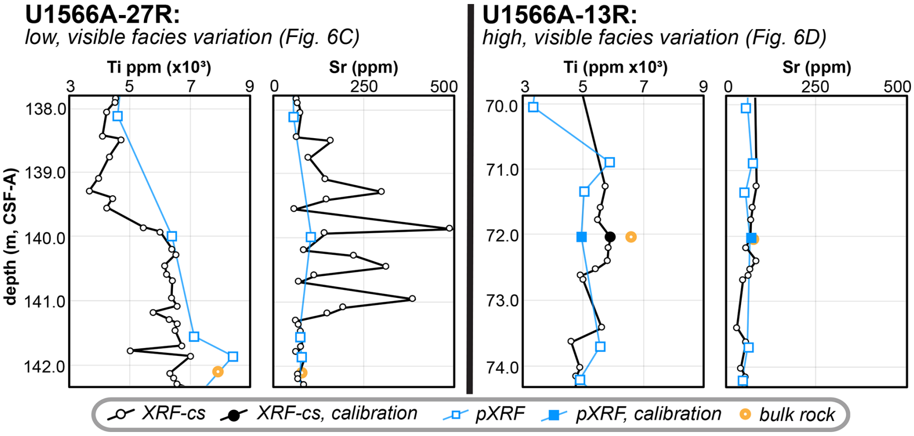

Figure 7. Ti and Sr calibrated concentration ($\mu g\, g^{-1}$) chemical stratigraphy plots for two core sections of Hole U1566A basalts. Section 13R (Fig. 6D) has high facies variability within the represented 4 m section, while Section 27R (Fig. 6C) is continuous aphyric basalt. The XRF-cs and pXRF labeled with "calibration" denote analyses that were used to calculate the calibration curves (Fig. S2).

6 Conclusions

The main goal of this study is to assess the quality of XRF-cs data collected for basaltic hard-rock cores and to evaluate their ability to capture geochemical variability for efficient sample selection. Overall, XRF-cs can rapidly provide higher-spatial-resolution chemical data relative to traditional methods. In this case study, the XRF-cs dataset, acquired in 4 d, is 280 % larger than the previously collected pXRF dataset. The chemical stratigraphy derived from XRF-cs data broadly shows good agreement with pXRF and bulk-rock datasets, indicating that it reliably reflects the true chemical variations in the cores measured. However, there are important considerations when using XRF-cs on hard-rock materials like basalt:

1. XRF-cs data must be carefully filtered to remove measurements affected by poor contact with the detector using the reported intensity of Ar as a quality indicator.

2. Geochemical trends in filtered, uncalibrated XRF-cs data are, in some cases, misleading in comparison to trends seen in other datasets, and so calibration is essential to ensure that the data accurately represent true chemical variability whenever possible.

3. If uncalibrated, XRF-cs data should be interpreted only through element intensity ratios as a first-order attempt to account for differences in mass attenuation between elements.

The utility of XRF-cs data for sample selection may be strongly dependent on the type of study the samples are being selected for. XRF-cs data measure more elements than usually reported on for pXRF analyses, which limits the number of elements that can be calibrated using the methods described here. However, this limitation could be eliminated by measuring a suite of SRMs with the XRF-cs alongside the cores being sampled (e.g., Planke et al., 2023a) or, potentially, with non-linear models for correlating element intensity with concentration, as described by Weltje et al. (2015). Our results suggest that large XRF-cs datasets can define regional-scale chemical variability better than pXRF datasets by increasing sampling resolution and reducing sampling bias. On the scale of local chemical stratigraphy, the high spatial resolution of the XRF-cs data can highlight small-scale variations missed by the more discrete methods. While the case study presented here only measures basaltic cores, these results suggest that it may be applied to other hard-rock cores in future applications.

Data availability. The XRF-cs data used in this paper are available as supplementary tables on Zenodo via https://doi.org/10.5281/zenodo.18343315 (Morris et al., 2026). The calibrated pXRF and bulk-rock ICP-MS data are available as a dataset in the GeoRoc database (https://doi.org/10.5880/digis.2025.011, Tegner et al., 2025).

Supplement. The supplement related to this article is available online at https://doi.org/10.5194/sd-35-21-2026-supplement.

Author contributions. AMM and SL designed the study. AMM performed the analyses and wrote the first draft of the paper. CAAZ trained AMM on the XRF core scanner. SL revised the first draft of the paper. All of the authors contributed to the final version of this paper.

Competing interests. The contact author has declared that none of the authors has any competing interests.

Acknowledgements. This work has benefited from discussions with J. Hertzberg at IODP Texas A&M University and with B. Kaiser and R. F. Shannon at Veracio during an NSF Non-Academic Research Internship for Graduate Students (INTERN) Supplemental Funding Opportunity. A. M. Morris also acknowledges support from the University of Utah Department of Geology and Geophysics Williamson Fellowship Program. The authors also acknowledge other members of the IODP Expedition 396 offshore Science Party, including C. Berndt, H. Brinkhuis, D. T. Harper, J. Longman, and G. T. F. Mohn, and thank the crew, drill team members, and lab technicians on board the RV *JOIDES Resolution* during the expedition. The authors also thank two anonymous reviewers for their time providing constructive comments which were implemented to improve the quality of this manuscript, as well as Thomas Wiersberg for his editorial handling.

Financial support. This research has been supported by the American Chemical Society Petroleum Research Fund (grant no. 61305-DNI8); the National Science Foundation, Directorate for Geosciences (grant nos. 1946346 and 1326927); the Natural Environment Research Council, National Centre for Earth Observation (grant no. NE/W004828/1); and the Norges Forskningsråd, SFI Offshore Mechatronics (grant no. 336293).

Review statement. This paper was edited by Thomas Wiersberg and reviewed by two anonymous referees.

References

Alvarez Zarikian, C. A., Yager, S. L., Harper, D. T., Christopoulou, M., Clementi, V. J., Varela, N., and Expedition 396 Scientists: Data Report: X-Ray Fluorescence Scanning of Site U1574, Vøring Plateau, IODP Expedition 396, Proceedings of the International Ocean Discovery Program, 396, https://doi.org/10.14379/iodp.proc.396.2023, 2024.

Bourke, A. and Ross, P.-S.: Portable X-ray fluorescence measurements on exploration drill-cores: Comparing performance on unprepared cores and powders for "whole-rock" analysis, Geochem. Explor. Environ. Anal., 16, 147–157, https://doi.org/10.1144/geochem2014-326, 2016.

Bowman, E. E. and Ducea, M. N.: Pyroxenite melting at subduction zones, Geology, 51, 383–386, https://doi.org/10.1130/G50929.1, 2023.

Dawson, H. L., Dubrule, O., and John, C. M.: Impact of dataset size and convolutional neural network architecture on transfer learning for carbonate rock classification, Comput. Geosci., 171, 105284, https://doi.org/10.1016/j.cageo.2022.105284, 2023.

Drake, B. L., MacDonald, B. L., and Shannon, R. F.: Introduction, In Advances in Portable X-Ray Fluorescence Spectrometry: Instrumentation, Application and Interpretation, Roy. Soc. Ch., 1–10, https://doi.org/10.1039/9781839162695-00001, 2022.

Dunlea, A. G., Murray, R. W., Tada, R., Alvarez-Zarikian, C. A., Anderson, C. H., Gilli, A., Giosan, L., Gorgas, T., Hennekam, R., Irino, T., Murayama, M., Peterson, L. C. Reichart, G.-J., Seki, A., Zheng, H., and Ziegler, M.: Intercomparison of XRF core scanning results from seven labs and approaches to practical calibration, Geochem. Geophys. Geosy., 21, e2020GC009248, https://doi.org/10.1029/2020GC009248, 2020.

Fisher, L., Gazley, M. F., Baensch, A., Barnes, S. J., Cleverley, J., and Duclaux, G.: Resolution of geochemical and lithostratigraphic complexity: A workflow for application of portable X-ray fluorescence to mineral exploration, Geochem. Explor. Environ. Anal., 14, 149–159, https://doi.org/10.1144/geochem2012-158, 2014.

Forster, N., Grave, P., Vickery, N., and Kealhofer, L.: Non-destructive analysis using PXRF: Methodology and application to archaeological ceramics, X-Ray Spectrom., 40, 389–398, https://doi.org/10.1002/xrs.1360, 2011.

Fresia, B., Ross, P.-S., Gloaguen, E., and Bourke, A.: Lithological discrimination based on statistical analysis of multi-sensor drill core logging data in the Matagami VMS district, Quebec, Canada, Ore Geol. Rev., 80, 552–563, https://doi.org/10.1016/j.oregeorev.2016.07.019, 2017.

Gebregiorgis, D., Giosan, L., Hathorne, E. C., Anand, P., Nilsson-Kerr, K., Plass, A., Lückge, A., Clemens, S. C., and Frank, M.: What Can We Learn From X-Ray Fluorescence Core Scanning Data? A Paleomonsoon Case Study, Geochem. Geophys. Geosy., 21, e2019GC008414, https://doi.org/10.1029/2019GC008414, 2020.

Hahn, A., Bowen, M. G., Clift, P. D., Kulhanek, D. K., and Lyle, M. W.: Testing the Analytical Performance of Handheld XRF Using Marine Sediments of IODP Expedition 355, Geol. Mag., 157, 956–60, https://doi.org/10.1017/S0016756819000189, 2020.

Hallberg, J. A.: A geochemical aid to igneous rock type identification in deeply weathered terrain, J. Geochem. Explor., 20, 1–8, https://doi.org/10.1016/0375-6742(84)90085-2, 1984.

Hubbell, J. H. and Seltzer, S. M.: X-Ray Mass Attenuation Coefficients NIST Standard Reference Database 126, National Institute of Standards and Technology, https://doi.org/10.18434/T4D01F, 2004.

Jansen, J. H. F., Van der Gaast, S. J., Koster, B., and Vaars, A. J.: CORTEX, a shipboard XRF-scanner for element analyses in split sediment cores, Marine Geology, 151, 143–153, https://doi.org/10.1016/S0025-3227(98)00074-7, 1998.

Jenkins, R.: X-Ray Fluorescence Analysis, X-ray Characterization of Materials, 171–209, https://doi.org/10.1002/9783527613748.ch3, 1999.

Johnston, R. M., Ryan, J. G., and Expedition 366 Scientists: pXRF and ICP-AES characterization of shipboard rocks and sediments: protocols and strategies, Proceedings of the International Ocean Discovery Program, 366 https://doi.org/10.14379/iodp.proc.366.2018, 2018.

Jonnalagadda, M. K., Belgrano, T. M., Ryan, J. G., Kempton, P. D., Evans, A. D., Grant, L. J. C., Teagle, D. A. H., Coggon, R. M., Reece, J., Sylvan, J. B., Williams, T. J., Estes, E. R., and the Expedition 390/393 Scientists: Data report: High downhole resolution portable X-ray fluorescence geochemistry of South Atlantic Transect basement cores, IODP Expeditions 390C, 395E, 390, and 393, in: South Atlantic Transect, edited by: Coggon, R. M., Teagle, D. A. H., Sylvan, J. B., Reece, J., Estes, E. R., Williams, T. J., Christeson, G. L., and the Expedition 390/393 Scientists, Proceedings of the International Ocean Discovery Program, 390/393, International Ocean Discovery Program, College Station, TX, https://doi.org/10.14379/iodp.proc.390393.2024, 2024.

Koppers, A. and Coggon, R. (Eds.): Exploring Earth by Scientific Ocean Drilling: 2050 Science Framework, International Ocean Discovery Program, 124, https://doi.org/10.6075/J0W66J9H, 2020.

Kunkelova, T., Jung, S. J. A., de Leau, E. S., Odling, N., Thomas, A. L., Betzler, C., Eberli, G. P., Alvarez-Zarikian, C. A., Alonso-García, M., Bialik, O. M., Blättler, C. L., Guo, J. A., Haffen, S., Horozal, S., Inoue, M., Jovane, L., Kroon, D., Lanci, L., Laya, J. C., Hui Mee, A. L., Nakakuni, M., Nath, B. N., Niino, K., Petruny, L. M., Pratiwi, S. D., Slagle, A. L., Su, X., Swart, P. K., Wright, J. D., Yao, Z., Young, J. R, Lindhorst, S., Stainbank, S., Rueggeberg, A., Spezzaferri, S., Carrasqueira, I., Hu, S., and Kroon, D.: A two-million-year record of low-latitude aridity linked to continental weathering from the Maldives, Prog. Earth Planet. Sci., 5, 86, https://doi.org/10.1186/s40645-018-0238-x, 2018.

Lang, O. I. and Lambart, S.: First-row transition elements in pyroxenites and peridotites: A promising tool for constraining mantle source mineralogy, Chem. Geo., 612, 121137, https://doi.org/10.1016/j.chemgeo.2022.121137, 2022.

Lokier, S. W. and Al Junaibi, M.: The petrographic description of carbonate facies: Are we all speaking the same language?, Sedimentology, 63, 1843–1885, https://doi.org/10.1111/sed.12293, 2016.

Meyer, R., Hertogen, J., Pedersen, R. B., Viereck-Götte, L., and Abratis, M.: Interaction of mantle derived melts with crust during the emplacement of the Vøring Plateau, N.E. Atlantic, Marine Geology, 261, 3–16, https://doi.org/10.1016/j.margeo.2009.02.007, 2009.

Morris, A. M., Lambart, S., Stearns M. A., Bowman J. R., Jones M. T., Mohn G. T. F., Andrews G. D. M., Millet J., Tegner

C., Chatterjee S., Frieling J., Guo P., Berndt C., Planke S., Alvarez Zarikian C. A., Betlem P., Brinkhuis H., Christopoulou M., Ferré E. C., Filina I. V., Harper D. T., Jolley D. W., Longman J., Scherer R. P., Varela N., Xu W., Yager S. L., Agarwal A., and Clementi V. J.: Evidence for Low-pressure Crustal Anatexis During the Northeast Atlantic Break-up, Geochem. Geophys. Geosy. 25, e2023GC011413, https://doi.org/10.1029/2023GC011413, 2024.

Morris, A., Lambart, S., Alvarez Zarikian, C., Millett, J., Jones, M., Planke, S., Betlem, P., Chatterjee, S., Christpoulou, M., Ferre, E., Filina, I., Frieling, J., Scherer, R., Varela, N., Xu, W., and Yager, S.: Supplement to: Recommendations for using core XRF data on basaltic cores as a tool to assess compositional variability, Zenodo [data set], https://doi.org/10.5281/zenodo.18343315, 2026.

Pälike, H., Shackleton, N. J., and Röhl, U.: Astronomical forcing in Late Eocene marine sediments, Earth Planet. Sci. Lett., 193, 589–602, https://doi.org/10.1016/S0012-821X(01)00501-5, 2001.

Pearce, J. A.: Immobile Element Fingerprinting of Ophiolites, Elements, 10, 101–108, https://doi.org/10.2113/gselements.10.2.101, 2014.

Pearce, J. A. and Norry, M. J.: Petrogenetic implications of Ti, Zr, Y, and Nb variations in volcanic rocks, Contrib. Mineral Petr., 69, 33–47, https://doi.org/10.1007/BF00375192, 1979.

Planke, S., Berndt, C., Alvarez Zarikian, C. A., Agarwal, A., Andrews, G. D. M., Betlem, P., Bhattacharya, J., Brinkhuis, H., Chatterjee, S., Christopoulou, M., Clementi, V. J., Ferré, E. C., Filina, I. Y., Frieling, J., Guo, P., Harper, D. T., Jones, M. T., Lambart, S., Longman, J., Millett, J. M., Mohn, G., Nakaoka, R., Scherer, R. P., Tegner, C., Varela, N., Wang, M., Xu, W., and Yager, S. L.: Expedition 396 methods, in: Mid-Norwegian Margin Magmatism and Paleoclimate Implications, edited by: Planke, S., Berndt, C., Alvarez Zarikian, C. A., and the Expedition 396 Scientists, Proceedings of the International Ocean Discovery Program, 396, International Ocean Discovery Program, College Station, TX, https://doi.org/10.14379/iodp.proc.396.2023, 2023a.

Planke, S., Berndt, C., Alvarez Zarikian, C. A., Agarwal, A., Andrews, G. D. M., Betlem, P., Bhattacharya, J., Brinkhuis, H., Chatterjee, S., Christopoulou, M., Clementi, V. J., Ferré, E. C., Filina, I. Y., Frieling, J., Guo, P., Harper, D. T., Jones, M. T., Lambart, S., Longman, J., Millett, J. M., Mohn, G., Nakaoka, R., Scherer, R. P., Tegner, C., Varela, N., Wang, M., Xu, W., and Yager, S. L.: Expedition 396 summary, in: Mid-Norwegian Margin Magmatism and Paleoclimate Implications, edited by: Planke, S., Berndt, C., Alvarez Zarikian, C. A., and the Expedition 396 Scientists, Proceedings of the International Ocean Discovery Program, 396, International Ocean Discovery Program, College Station, TX, https://doi.org/10.14379/iodp.proc.396.2023, 2023b.

Planke, S., Berndt, C., Alvarez Zarikian, C. A., Agarwal, A., Andrews, G. D. M., Betlem, P., Bhattacharya, J., Brinkhuis, H., Chatterjee, S., Christopoulou, M., Clementi, V. J., Ferré, E. C., Filina, I. Y., Frieling, J., Guo, P., Harper, D. T., Jones, M. T., Lambart, S., Longman, J., Millett, J. M., Mohn, G., Nakaoka, R., Scherer, R. P., Tegner, C., Varela, N., Wang, M., Xu, W., and Yager, S. L.: Site U1566, in: Mid-Norwegian Margin Magmatism and Paleoclimate Implications, edited by: Planke, S., Berndt, C., Alvarez Zarikian, C. A., and the Expedition 396 Scientists, Proceedings of the International Ocean Discovery Program, 396, International Ocean Discovery Program, College Station, TX, https://doi.org/10.14379/iodp.proc.396.104.2023, 2023c.

Planke, S., Berndt, C., Alvarez Zarikian, C. A., Agarwal, A., Andrews, G. D. M., Betlem, P., Bhattacharya, J., Brinkhuis, H., Chatterjee, S., Christopoulou, M., Clementi, V. J., Ferré, E. C., Filina, I. Y., Frieling, J., Guo, P., Harper, D. T., Jones, M. T., Lambart, S., Longman, J., Millett, J. M., Mohn, G., Nakaoka, R., Scherer, R. P., Tegner, C., Varela, N., Wang, M., Xu, W., and Yager, S. L.: Sites U1571 and U1572, in: Mid-Norwegian Margin Magmatism and Paleoclimate Implications, edited by: Planke, S., Berndt, C., Alvarez Zarikian, C. A., and the Expedition 396 Scientists, Proceedings of the International Ocean Discovery Program, 396, International Ocean Discovery Program, College Station, TX, https://doi.org/10.14379/iodp.proc.396.107.2023, 2023d.

Planke, S., Berndt, C., Alvarez Zarikian, C. A., Agarwal, A., Andrews, G. D. M., Betlem, P., Bhattacharya, J., Brinkhuis, H., Chatterjee, S., Christopoulou, M., Clementi, V. J., Ferré, E. C., Filina, I. Y., Frieling, J., Guo, P., Harper, D. T., Jones, M. T., Lambart, S., Longman, J., Millett, J. M., Mohn, G., Nakaoka, R., Scherer, R. P., Tegner, C., Varela, N., Wang, M., Xu, W., and Yager, S. L.: Site U1574, in: Mid-Norwegian Margin Magmatism and Paleoclimate Implications, edited by: Planke, S., Berndt, C., Alvarez Zarikian, C. A., and the Expedition 396 Scientists, Proceedings of the International Ocean Discovery Program, 396, International Ocean Discovery Program, College Station, TX, https://doi.org/10.14379/iodp.proc.396.109.2023, 2023e.

Reagan, M. K., Pearce, J. A., Petronotis, K., Almeev, R., Avery, A. A., Carvallo, C., Chapman, T., Christeson, G. L., Ferré, E. C., Godard, M., Heaton, D. E., Kirchenbaur, M., Kurz, W., Kutterolf, S., Li, H. Y., Li, Y., Michibayashi, K., Morgan, S., Nelson, W. R., Prytulak, J., Python, M., Robertson, A. H. F., Ryan, J. G., Sager, W. W., Sakuyama, T., Shervais, J. W., Shimizu, K., and Whattam, S. A.: Expedition 352 methods, in: Izu-Bonin-Mariana Fore Arc, edited by: Reagan, M. K., Pearce, J. A., Petronotis, K., and the Expedition 352 Scientists, Proceedings of the International Ocean Discovery Program, 352, International Ocean Discovery Program, College Station, TX, https://doi.org/10.14379/iodp.proc.352.102.2015, 2015a.

Reagan, M. K., Pearce, J. A., Petronotis, K., Almeev, R., Avery, A. A., Carvallo, C., Chapman, T., Christeson, G. L., Ferré, E. C., Godard, M., Heaton, D. E., Kirchenbaur, M., Kurz, W., Kutterolf, S., Li, H. Y., Li, Y., Michibayashi, K., Morgan, S., Nelson, W. R., Prytulak, J., Python, M., Robertson, A. H. F., Ryan, J. G., Sager, W. W., Sakuyama, T., Shervais, J. W., Shimizu, K., and Whattam, S. A.: Expedition 352 summary, in: Izu-Bonin-Mariana Fore Arc, edited by: Reagan, M. K., Pearce, J. A., Petronotis, K., and the Expedition 352 Scientists, Proceedings of the International Ocean Discovery Program, 352, International Ocean Discovery Program, College Station, TX, https://doi.org/10.14379/iodp.proc.352.101.2015, 2015b.

Richter, T. O., Van Der Gaast, S., Koster, B., Vaars, A., Gieles, R., De Stigter, H. C., De Haas, H., and Van Weering, T. C. E.: The Avaatech XRF Core Scanner: Technical description and applications to NE Atlantic sediments, Geo. Soc. Spec. Publ., 267, 39–50, https://doi.org/10.1144/GSL.SP.2006.267.01.03, 2006.

Romano, P., Brusca, L., and Liotta, M.: Element mobility during basalt-water-CO2 interaction: Observations in natural systems vs. laboratory experiments and implication for carbon storage, Geochem. T., 25, 4, https://doi.org/10.1186/s12932-024-00087-7, 2024.

Rothwell, R. G. and Croudace, I. W.: Micro-XRF Studies of Sediment Cores: A Perspective on Capability and Application in the Environmental Sciences, in: Micro-XRF Studies of Sediment Cores, edited by: Croudace, I. W. and Rothwell, R. G., Dev. Paleoenviron. Res., 17, https://doi.org/10.1007/978-94-017-9849-5_1, 2015.

Ryan, J. G., Shervais, J. W., Li, Y., Reagan, M. K., Li, H. Y., Heaton, D., Godard, M., Kirchenbaur, M., Whattam, S. A., Pearce, J. A., Chapman, T., Nelson, D., Prytulak, J., Shimizu, K., Petronotis, K., and the IODP Expedition 352 Scientific Team: Application of a handheld X-ray fluorescence spectrometer for real-time, high-density quantitative analysis of drilled igneous rocks and sediments during IODP Expedition 352, Chem. Geol., 451, 55–66, https://doi.org/10.1016/j.chemgeo.2017.01.007, 2017.

Sato, H.: Nickel content of basaltic magmas: Identification of primary magmas and a measure of the degree of olivine fractionation, Lithos, 10, 113–120, https://doi.org/10.1016/0024-4937(77)90037-8, 1977.

Siegel, A. F. and Wagner, M. R.: ANOVA: Testing for Differences Among Many Samples and Much More, in: Practical Business Statistics, 8th edn., 485–510, https://doi.org/10.1016/B978-0-12-820025-4.00015-4, 2022.

Sitko, R. and Zawisza, B.: Quantification in X-Ray Fluorescence Spectrometry, in: X-Ray Spectroscopy, edited by: Sharma, S. K., InTech, 137–162, https://doi.org/10.5772/29367, 2012.

Smith, R. E. and Smith, S. E.: Comments on the use of Ti, Zr, Y, Sr, K, P and Nb in classification of basaltic magmas, Earth Planet. Sc. Lett., 32, 114–120, https://doi.org/10.1016/0012-821X(76)90049-2, 1976.

Sun, S.-S., Nesbitt, R. W., and Sharaskin, A. Ya.: Geochemical characteristics of mid-ocean ridge basalts. Earth Planet. Sc. Lett., 44, 119–138, https://doi.org/10.1016/0012-821X(79)90013-X, 1979.

Super, J.: Looking toward the future of ocean drilling, Nature Geoscience, 17, 1189–1192, https://doi.org/10.1038/s41561-024-01600-4, 2024.

Tegner, C., Guo, P., Chatterjee, S., Lambart, S., Jones, M. T., Planke, S., Neumann, E.-R., Svensen, H. H., Lesher, C. E., Cashman, K., Takahashi, T., Cunningham, E. H., Morris, A. M., Stokke, E. W., Millet, J. M., Mohn, G. T. F., Longman, J., Berndt, C., Alvarez Zarikian, C. A., Betlem, P., Brinkhuis, H., Christopoulou, M., Ferré, E., Filina, I., Frieling, J., Harper, D. T., Scherer, R. P., Varela, N., Xu, W., and Yager, S. L.: New geochemical analyses on samples drilled on the mid-Norwegian margin during IODP Expedition 396, ODP Leg 104 and DSDP Leg 38, GFZ Data Services [data set], https://doi.org/10.5880/digis.2025.011, 2025.

Virtanen, P., Gommers, R., Oliphant, T. E., Haberland, M., Reddy, T., Cournapeau, D., Burovski, E., Peterson, P., Weckesser, W., Bright, J., van der Walt, S. J., Brett, M., Wilson, J., Millman, K. J., Mayorov, N., Nelson, A. R. J., Jones, E., Kern, R., Larson, E., Carey, C. J., Polat, I., Feng, Y., Moore, E. W., VanderPlas, J., Laxalde, D., Perktold, J., Cimrman, R., Henriksen, I., Quintero, E. A., Harris, C. R., Archibald, A. M., Ribeiro, A. H., Pedregosa, F., van Mulbregt, P., and SciPy 1.0 Contributors: SciPy 1.0: Fundamental algorithms for scientific computing in Python, Nat. Methods, 17, 261–272, https://doi.org/10.1038/s41592-019-0686-2, 2020.

Vlag, P. A., Kruiver, P. P., and Dekkers, M. J.: Evaluating climate change by multivariate statistical techniques on magnetic and chemical properties of marine sediments (Azores region), Palaeogeography, Palaeoclimatology, Palaeoecology, 212, 23–44, https://doi.org/10.1016/j.palaeo.2004.05.015, 2004.

Wang, J., Su, B.-X., Robinson, P. T., Xiao, Y., Bai, Y., Liu, X., Sakyi, P. A., Jing, J.-J., Chen, C., Liang, Z., and Bao, Z.-A.: Trace elements in olivine: Proxies for petrogenesis, mineralization and discrimination of mafic-ultramafic rocks,. Lithos, 388–389, 106085, https://doi.org/10.1016/j.lithos.2021.106085, 2021.

Weltje, G. J. and Tjallingii, R.: Calibration of XRF core scanners for quantitative geochemical logging of sediment cores: Theory and application, Earth Planet. Sc. Lett., 274, 423–438, https://doi.org/10.1016/j.epsl.2008.07.054, 2008.

Weltje, G. J., Bloemsma, M. R., Tjallingii, R., Heslop, D., Röhl, U., and Croudace, I. W.: Prediction of geochemical composition from XRF core scanner data: a new multivariate approach including automatic selection of calibration samples and quantification of uncertainties, in: Micro-XRF Studies of Sediment Cores: Applications of a non-destructive tool for the environmental sciences, Springer Netherlands, Dordrecht, 507–534, https://doi.org/10.1007/978-94-017-9849-5_21, 2015.